Volume 1 | Number 1 | Jan 2013 | Pages 1–100

Journal of
Materials Chemistry C

Materials for optical and electronic devices
www.rsc.org/materialsC

ROYAL SOCIETY
OF CHEMISTRY

ROYAL SOCIETY
OF CHEMISTRY

www.rsc.org/materialsC

Journal Name

ARTICLE

Morphological and crystal structural control of tungsten trioxide for highly sensitive NO$_2$ gas sensors

Zhicong Meng,[a] Aya Fujii,[a] Takeshi Hashishin,[b] Noriyuki Wada,[c] Tomoe Sanada,[a] Jun Tamaki,[a] Kazuo Kojima,[a*] Hitoshi Haneoka[d] and Takeyuki Suzuki[d]

We discussed the synthesis of cuboid-monoclinic tungsten oxide (C-m-WO$_3$) and particles and hexagonal-plate-like-hexagonal tungsten oxide (H-h-WO$_3$) particles by acidification and hydrothermal treatment with $(NH_4)_{10}W_{12}O_{41} \cdot 5H_2O$ as a starting material. From the WO$_3$ particles, thin- and thick-film gas sensors were fabricated for NO$_2$ sensing application, and the effect of morphology and crystal structure of the WO$_3$ particles on the NO$_2$ sensing properties was investigated. The extremely high sensor responses of 160 to 20-ppb NO$_2$ and of 10120 to 500-ppb NO$_2$ were obtained for a C-m-WO$_3$ thin-film sensor at operating temperature of 200 ºC. The crystal structure features of as-prepared particles were studied by XRD, XPS, SEM, TEM, and solid state ^1H and ^{13}C NMR measurements. The presence of residual impurities, cations, and high density of surface OH$^-$ in the H-h-WO$_3$ particles was demonstrated, which could be one of the key reasons for the crystal structure dependence of the sensing properties in C-m-WO$_3$ and H-h-WO$_3$ gas sensors.

Introduction

Nanostructured materials are considered as good candidates for gas-sensing applications. Gas sensors based on nanostructures of oxide semiconductors such as tin oxide,[1,2] zinc oxide,[3] indium oxide,[4] and tungsten oxide[5,6] have shown enhanced capability to detect target gases with higher sensitivity, faster response-recovery and lower operating temperatures. Tungsten trioxide (WO$_3$) is a versatile material which offers manifold applications owing to its promising physical and chemical properties. As an n-type semiconductor, WO$_3$ is a potential candidate to be used in photo-electrochemical cells.[7] In contrast to TiO$_2$, which absorbs only UV light, WO$_3$ possesses a relatively small band gap between 2.4 and 2.8 eV, which makes it a visible-light-responsive photocatalyst.[8,9] With the ability to change its colour easily, WO$_3$ is the most researched material for chromogenic devices.[10-12] For semiconductor gas sensors, WO$_3$ is an important base oxide which exhibits high sensitivity to non-hydrocarbon gases such as NO$_2$, O$_3$, H$_2$S and NH$_3$.[13-15] In particular, WO$_3$ showed superior sensitivity and selectivity in detecting NO$_2$ gas.[16-18] So far enhanced gas-sensing properties of nanostructure WO$_3$ to NO$_2$ have been observed for various types of morphology such as nanosheets assembled hollow microspheres,[19] square-like nanostructures,[20] Lamellar structures,[21] spherical nanoparticles,[22] nanorod bundles,[23] nanowires,[24] nanowires array[25] and three-dimensional nanowire networks.[26] These WO$_3$ nanostructures have been prepared in several ways: acidification and hydrothermal treatment, aerosol-assisted CVD and thermal evaporation. On the other hand, WO$_3$ has several crystalline modifications: triclinic, monoclinic, orthorhombic, hexagonal, and cubic. Up to now, most of the reports on gas sensor applications are of monoclinic WO$_3$ (m-WO$_3$),[19-23, 25-26] while hexagonal WO$_3$ (h-WO$_3$) has been studied for sensing NH$_3$ or H$_2$S only by a few groups,[24,27-30] where the h-WO$_3$ prepared by acidic precipitation followed by hydrothermal and heat treatments at low temperatures or by annealing hexagonal ammonium tungsten bronze (HATB). Recently it has been revealed that the crystal structure (monoclinic or hexagonal) of the WO$_3$ caused large differences not only in sensing properties,[31] but also in activities of WO$_3$-supporting catalysis.[32]

Among these reports, the interaction between WO$_3$ and gases is significant to understand the correlation between gas-sensing behavior and surface state of WO$_3$. The oxidation state of tungsten atoms in h-WO$_3$ observed with XPS and the gas-sensing property of the h-WO$_3$ to 10-ppm H$_2$S have been reported.[28,31] The sensor responses (the ratio of conductance in the air to that in H$_2$S) to 10-ppm H$_2$S for an oxidized h-WO$_3$ (W^{6+}:96.8, W^{5+}:1.8, and W^{4+}:1.4%) and a reduced h-WO$_3$ (W^{6+}:77.3, W^{5+}:15.9, and W^{4+}:6.8%) at 200 ºC had similar values of 41 and 44, respectively. However, the response time was longer for the reduced h-WO$_3$ than for the oxidized h-WO$_3$. It is considered that on the outermost surface of h-WO$_3$, the amount of oxygen defects for W^{5+} is less than that for W^{6+}, thus the response time becomes longer for reducing H$_2$S gas. It is interestingly stated that in the h-WO$_3$ sensing property to 50-ppm NH$_3$, the conduction type of h-WO$_3$ at 200 ºC is changed from that at 100 ºC.[30] Tungsten vacancies contribute to generation of holes at 100 ºC, however, in reducing NH$_3$ gas, a depletion layer increases (the resistance increases) by accompanying disappearance of holes. On the other hand, on the outermost surface of h-WO$_3$, the W-O bond is transiently broken, and oxygen vaporizes to generate oxygen vacancies. In order to keep a charge balance, in the depletion layer of the outermost surface, the small amount of charge carriers (holes) generate an inversion layer within the depletion layer, however, electrons flow into the inversion layer to remove that layer. Then, the supply of free electrons from NH$_3$ decreases the resistance. The sensor responses as the resistance ratios to 50-ppm NH$_3$ at 100 and 200 ºC were 2.7 and 1.2, respectively. Other gas-sensing studies with h-WO$_3$ were few; only the sensor responses to 50-ppm NH$_3$ at 300 ºC were reported to be 1.6[29] and 3.0.[32] Another interesting study is that the OH density on the surface is higher for m-WO$_3$ than for h-WO$_3$;[32] those high OH density sites on the surface of WO$_3$ are beneficial for Au nanoparticle nucleation, leading to that the CO oxidation ability is larger for Au deposited m-WO$_3$ than for Au

deposited h-WO$_3$. As described above, it is said that the surface properties of WO$_3$ affect greatly the gas-sensing and catalytic properties.
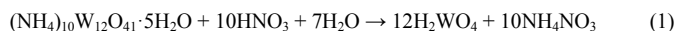
In the present study, we discuss two kinds of WO$_3$ nanostructure with differences in morphology and crystal structure: cuboid-monoclinic WO$_3$ (C-m-WO$_3$) and hexagonal-plate-like-hexagonal WO$_3$ (H-h-WO$_3$), synthesized by acidification and hydrothermal treatment using the same starting material of ammonium paratungstate pentahydrate, and discuss also their NO$_2$ gas-sensing properties. Our study aims to investigate how the morphology (cuboid: C- or hexagonal-plate: H-) and crystal structure (m- or h-) of WO$_3$ influence the sensing properties.

Experimental Section

Synthesis

A facile hydrothermal process was employed to synthesize C-m-WO$_3$ and H-h-WO$_3$. Ammonium paratungstate pentahydrate ((NH$_4$)$_{10}$W$_{12}$O$_{41}$·5H$_2$O) and nitric acid (69 %) were used as starting materials for both samples. In synthesizing the C-m-WO$_3$ sample, (NH$_4$)$_{10}$W$_{12}$O$_{41}$·5H$_2$O was dissolved in deionized water, and heated to 80 °C to form transparent solution with mild stirring. Then HNO$_3$ was added into the solution drop by drop, and the solution was kept stirring at 75 °C for 25 min. After the reaction was completed, the resulting product was centrifuged and washed with deionized water. The precipitate (precursor I: H$_2$WO$_4$) was transferred into 50 ml deionized water to be stirred for 24 h at room temperature. Then the suspension was transferred to a 100-ml Teflon-lined stainless-steel autoclave and kept at 160 °C for 14 h. After naturally cooling to room temperature, the collected product was dried at 35 °C for 48 h. Then the as-prepared products were calcined at 400 °C for 3 h to obtain the final product of C-m-WO$_3$ particles.

In synthesizing the H-h-WO$_3$ sample, the aqueous solution of (NH$_4$)$_{10}$W$_{12}$O$_{41}$·5H$_2$O was heated to 70 °C, and HNO$_3$ was added at one fling. Then the reaction solution was naturally cooled down to room temperature. After centrifuged and washed with deionized water, the precipitate (precursor II: H$_2$WO$_4$) was transferred into 50 ml deionized water and added surfactant of cetyltrimethylammonium bromide ([CH$_3$(CH$_2$)$_{15}$N(CH$_3$)$_3$]Br, CTAB). After stirring for 3 h at room temperature, the suspension was hydrothermally treated at 150 °C for 10 h. After naturally cooling to room temperature, the collected product was washed, dried and calcined at 400 °C for 3 h to obtain the final product of H-h-WO$_3$ particles. The formation process of the two kinds of WO$_3$ can be described by the following reactions:

$$(NH_4)_{10}W_{12}O_{41}·5H_2O + 10HNO_3 + 7H_2O \rightarrow 12H_2WO_4 + 10NH_4NO_3 \quad (1)$$

$$H_2WO_4 \rightarrow WO_3 + H_2O \quad (2)$$

Characterization

The crystal phases of the hydrothermally synthesized samples as well as their precursors were studied by powder X-ray diffraction (XRD) using CuKα radiation (Rint-2200, Rigaku, Japan). The morphology of the WO$_3$ particles was investigated by field-emission scanning electron microscopy (FE-SEM) (S-4800, Hitachi, Japan), and transmission electron microscopy (TEM, JEM-2100F, JEOL, Japan) operated at 200 kV. The specific surface area (a$_{BET}$) and pore size distribution of the hydrothermally synthesized samples were measured with Brunauer-Emmett-Teller (BET) method (BELSORP 18, BEL, Japan). Solid-state ^{1}H and ^{13}C NMR spectra were recorded on an NMR spectrometer (Bruker, AVANCE III, 600WB, SSNMR) with a 4.0-mm low-gamma probe. The pulse program for ^{1}H MAS (magic angle spinning) NMR was CRAMPS with the MAS rate of 2.3 kHz, and that for ^{13}C MAS NMR was DDMAS with the MAS

rate of 12 kHz. Chemical shifts were referenced to glycine (δ^1H = 7 ppm, δ^{13}C = 176 ppm). The measurements of the ^{1}H-CRAMPS NMR and the ^{13}C-DDMAS NMR took 10 min and 14 h, respectively, for each C-m-WO$_3$ and H-h-WO$_3$ sample. X-ray photoelectron spectra (XPS) from the surface of the samples were recorded on an instrument (ULVAC, PHI, ESCA, 5450LC) using MgKα radiation. The spectrometer was calibrated with the binding energy of the C 1s line (285 eV).
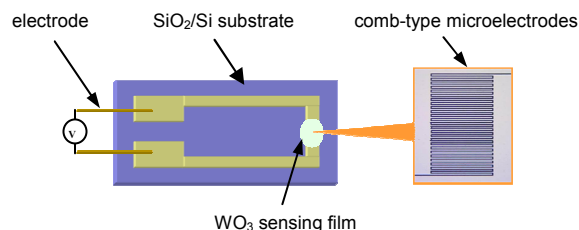
NO$_2$ sensor fabrication and measurement

Figure 1. Configuration of a WO$_3$ sensor.

An SiO$_2$/Si substrate equipped with Au comb-type microelectrodes was used for NO$_2$ sensing measurements. The configuration of a sensor is shown in Fig. 1. The area of the comb-type microelectrodes was 0.3×0.5 mm^2, where both the strip width of a finger and the distance between the adjacent fingers were 5 μm. The as-synthesized WO$_3$ powders were dispersed into the hydrophobic solvent of 1,2-pentanediol and kept with stirring for 7 days to obtain highly dispersive suspensions used for sensing film formation. The as-obtained suspension was deposited onto the comb-type microelectrodes with a micro-injector for thin-film sensor and with a micropipette for thick-film one, dried, and then calcined in air at 400 °C for 3 h to form a WO$_3$ sensing film. The thickness of the sensing film could be controlled in the range of 1.6 – 3.0 μm for thin-film sensor and 10 – 15 μm for thick-film one by changing the WO$_3$ powder content in suspension and the dropping amount of suspension. Gas sensing experiments were carried out in a conventional flow apparatus equipped with a heating facility at a gas flow rate of 100 cm^3/min. The concentration of NO$_2$ was varied between 0.02 and 1 ppm by diluting a parent NO$_2$ gas (5.01 ppm in N$_2$) with oxygen and dry air. The sensor response (S) was defined as the ratio of Rg to Ra (S = Rg/Ra), where Rg is the electric resistance in NO$_2$-containing air, and Ra is that in air. The schematic diagram of sensing measurement equipment is drawn in Fig. S1.

Results and discussion

Material characteristics

Fig. 2 shows the XRD patterns of the as-obtained WO$_3$ samples and the precursors I and II (H$_2$WO$_4$). All typical diffraction peaks for the C-m-WO$_3$ sample can be readily indexed to monoclinic phase (JCPDS No. 83-0950). No characteristic peaks from other crystalline impurities were detected, which indicates that the C-m-WO$_3$ is single, monoclinic phase. The diffraction peaks of the H-h-WO$_3$ sample correspond to hexagonal phase (JCPDS No. 33-1387) and monoclinic one (JCPDS No. 83-0950). The patterns of the precursors I and II almost agree with those of orthorhombic H$_2$WO$_4$ (JCPDS No. 43-0679) reported previously,[33] and the pattern of the precursor II shows the preferentially oriented (2 0 0) plane, compared to the precursor I. The morphology of the as-synthesized WO$_3$ particles is shown in Fig. 3. The grain size distribution estimated from the FE-SEM image was 50 – 200 nm for the cuboid-shaped C-m-WO$_3$ sample. The H-h-WO$_3$ sample consisted mainly of hexagonal-plate-shaped particles that are about 1000 – 2000 nm in length and 20 – 30 nm in thickness, together

with a minor amount of cuboid-shaped WO_3 particles with grain size distribution of about 20 – 100 nm. The particle sizes measured by TEM (Fig. 4) are the same as found by FE-SEM. The HR-TEM images revealed that both kinds of WO_3 particles were highly crystalline. Lattice fringes were clearly observed with a gap of 0.37 nm for the C-m-WO_3 particles, which was identified as the crystal panel of (2 0 0) of monoclinic-phase WO_3. For the H-h-WO_3 particles, the lattice distance was observed as 0.63 nm, which corresponded to the interspace of (1 0 0) planes of hexagonal-phase WO_3. Some defects were observed on the surface of the H-h-WO_3 particles. The BET specific surface areas of the samples obtained by N_2 adsorption were 11.7 and 4.87 m^2g^{-1}, and the average pore sizes were 18.3 and 37.7 nm for the C-m-WO_3 and H-h-WO_3 samples, respectively.
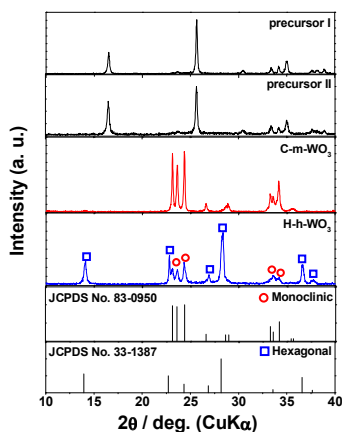

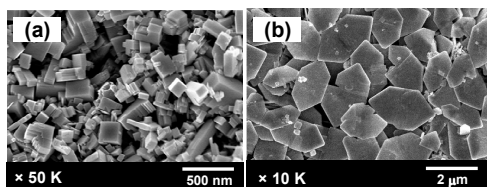Figure 2. XRD patterns of as-prepared WO_3 particles and the precursors I and II (H_2WO_4).

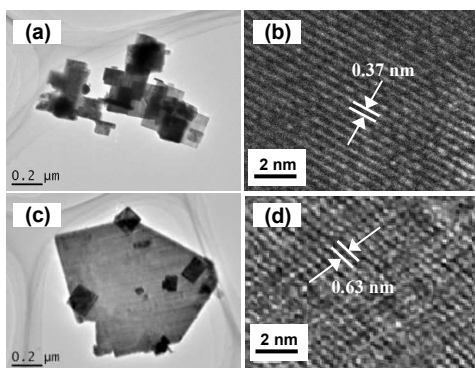Figure 3. FE-SEM images of (a) C-m-WO_3 and (b) H-h-WO_3.

Figure 4. TEM (a, c) and HR-TEM (b, d) images of the C-m-WO_3 (a, b) and H-h-WO_3 (c, d) particle.

NO_2 sensing properties

The NO_2 gas sensing properties of the C-m-WO_3 and H-h-WO_3 sensors were investigated with NO_2 concentrations ranging from 20 ppb to 1 ppm at operating temperatures ranging from 60 to 300 °C.

The temperature dependence of the sensor response to 0.5-ppm NO_2 shown in Fig. 5 indicated that the optimum operating temperature of the two thin-film sensors was 200 °C, which was the same as the thick-film sensors (data not shown). The H-h-WO_3 thin-film sensor showed higher response compared with the C-m-WO_3 one in a low temperature range of 60 – 120 °C. However, we noticed that without the desorption treatment, the sensor cannot recover the initial resistance after the NO_2 gas was turned off at the operating temperatures lower than 150 °C. Fig. 6 shows the transient response of the two thin-film sensors to 0.5-ppm NO_2 at the operating temperature of 200 °C. The electric resistance of the two sensors significantly increased upon exposure to NO_2 gas and recovered the initial value when the sensor was refreshed by dry air. This result indicated that the adsorption of NO_2 gas on the WO_3 sensing films was reversible. The C-m-WO_3 thin-film sensor exhibits a relatively long response time, though the recovery time of less than one minute was effective for the online monitoring of environmental, dilute NO_2. On the other hand, the H-h-WO_3 thin-film sensor performed with short response and long recovery times and a relatively high value of Ra (~10^6 Ω in RT, dry air) compared to the C-m-WO_3 one (~10^5 Ω in RT, dry air). Fig. 7 shows the sensor responses of the thin- and thick-film sensors at 200 °C as a function of NO_2 concentration. The logarithm of the sensor responses almost linearly increased with
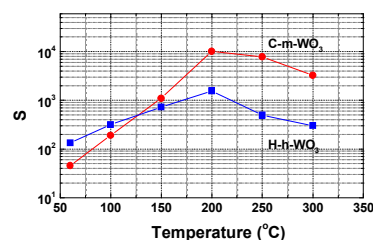

Figure 5. Temperature dependence of S for thin-film sensors of C-m-WO_3 and H-h-WO_3 to 0.5-ppm NO_2.
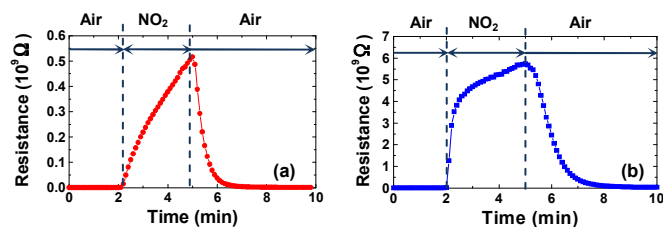

Figure 6. Typical response and recovery transients to 0.5-ppm NO_2 at 200 °C for thin-film sensors of (a) C-m-WO_3 and (b) H-h-WO_3.
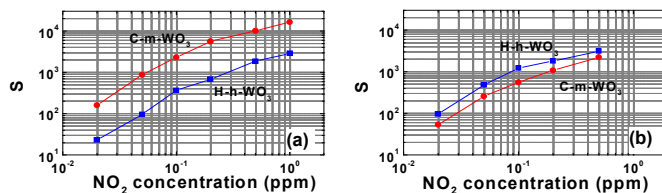

Figure 7. S as a function of NO_2 concentration for thin-film (a) and thick-film (b) sensors of C-m-WO_3 and H-h-WO_3 at 200 °C.
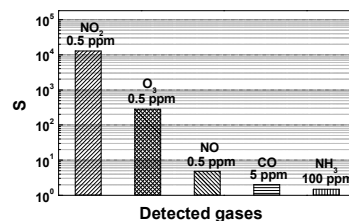

Figure 8. Sensor response of the C-m-WO_3 sensor to different gases measured at 200 °C.

Table I. Sensing properties of the thin- and thick-film sensors of C-m-WO$_3$ and H-h-WO$_3$ to NO$_2$ at the operating temperature of 200 °C.

WO$_3$ sensor	Thickness (μm)	Response (min: T$_{90}$)	Recovery (min: T$_{90}$)	S$_{20\text{-ppb NO}_2}$
C-m-WO$_3$ (thin)	2.19	2.4	0.8	160
H-h-WO$_3$ (thin)	2.17	1.9	1.8	23
C-m-WO$_3$ (thick)	11.5	1.3	0.9	43
H-h-WO$_3$ (thick)	14.4	1.4	2.4	96

Table II. NO$_2$ sensor response of different WO$_3$ nanostructures.

WO$_3$ nanostructures	Operating temp. (°C)	NO$_2$ conc. (ppb)	Sensor response (S = R$_{\text{NO}_2}$ / R$_{\text{air}}$)	Refs.
Hollow microspheres	300	1000	53.9	19
Square-like structures	125	100	92	20
Lamellar-structured particles	200	1000	275	21
Spherical particles	150	200	81	22
Porous nanorod bundles	250	5000	111.3	23
Nanowires	100	3000	38	24
Nanowire array	180	1000	10	25
C-m-WO$_3$ and H-h-WO$_3$ (Max.)	200	20	160, 96	This work
	200	500	10120, 3100	This work

the logarithm of the NO$_2$ concentration. It was indicated that for the thin-film sensors, sensor response of the C-m-WO$_3$ sensor was much higher than the H-h-WO$_3$ one, which was in contrast to the case of the corresponding thick-film sensors. The sensing properties of the four WO$_3$ sensors are summarized in Table I, where the 90 % response and recovery times were calculated from the resistance-time data based on the resistance when exposed to 0.5-ppm NO$_2$ for 3 min. The highest sensor response of 160 to 20-ppb NO$_2$ was obtained for the C-m-WO$_3$ thin-film sensor. Referring to some recent reports on the NO$_2$ sensing properties of different WO$_3$ nanostructures, as summarized in Table II, the C-m-WO$_3$ thin-film sensor fabricated in this work possesses very high sensor response to dilute NO$_2$. According to the environmental standard of NO$_2$ (less than 0.04 – 0.06 ppm per hour, in Japan), gas sensors should be able to detect NO$_2$ at the 10-ppb concentration level when used for the sensitive environmental monitoring at polluted areas caused by NO$_2$ emissions mainly from diesel vehicles. Both sensitivity (sensor response) and speed (response-recovery time) of the as-fabricated C-m-WO$_3$ sensor well satisfy the requirement for actual applications in high sensitive, environmental NO$_2$ monitoring.

Selectivity is another important factor of gas sensors in practical application. Fig. 8 shows the C-m-WO$_3$ sensor response to various gases of NO$_2$, O$_3$, NO, CO, and NH$_3$. The sensor exhibited the highest response to NO$_2$ gas among the gases. For actual applications in environmental monitoring, the effect from O$_3$ should be taken into consideration. Practical evaluation using a C-m-WO$_3$ sensor has demonstrated its sufficient stability, accuracy and resolution in a 10-week sequential measurement,[34] suggesting the great potential for actual environmental monitoring of dilute NO$_2$.

For most of the semiconductor oxide gas sensors, the change in electric resistance is primarily caused by the adsorption and reaction of the gas molecules on the surface of the sensing material. In the air, WO$_3$ particles adsorb oxygen molecules on the surface and generate chemisorbed oxygen species such as O^{2-}, O$^-$, and O$_2^-$. A depletion layer is formed on the surface area of WO$_3$ particles.[35] Upon exposure to NO$_2$ gas, the NO$_2$ molecules are adsorbed on the active sites on the WO$_3$ surface. Charge transfer is likely to occur from WO$_3$ to adsorbed NO$_2$ according to the following reactions,[36, 37] leading to the increase in thickness of the depletion layer.

$$NO_2\ (g) + e^- \rightarrow NO_2^-\ (ads) \tag{3}$$

$$NO_2\ (g) + e^- \rightarrow NO^-\ (ads) + O\ (ads) \tag{4}$$

In the C-m-WO$_3$ thin-film sensor, the enhanced sensing properties may be ascribed to the large specific surface area and the high crystallinity of the C-m-WO$_3$ particles consisted chiefly of the single-crystal WO$_3$. The specific surface area of the as-prepared C-m-WO$_3$ particles was 10 times larger than that of the normal commercially-supplied WO$_3$ (around 1 m^{2}g^{-1}), which significantly enhanced the adsorption sites on the surface of the sensing film.

Further the high crystallinity of the C-m-WO$_3$ particles provided efficient transport of electrons, resulting in the greatly improved sensing properties. On the other hand, the H-h-WO$_3$ showed much larger average pore size, which was about two times as large as that of the C-m-WO$_3$, and thus could form a porous-structure sensing film. In a thick-film sensor, the good porosity enhanced the diffusion of NO$_2$ in the sensing film and made NO$_2$ gas reach the deeper inner layer to be effectively adsorbed on WO$_3$ particles between electrodes, increasing the sensor resistance and thus inducing the high sensitivity. Compared to the H-h-WO$_3$, the high-densely packed C-m-WO$_3$ sensing film suppressed the diffusion of the gas molecules and made the NO$_2$ difficult to reach deep inside the sensing film. This might be the reason for the higher sensor response of the H-h-WO$_3$ thick-film sensor than the C-m-WO$_3$ thick-film one (Table I).

Thickness effect on the sensor response and the mechanism which related to the oxygen partial pressure has been reported for WO$_3$ sensors based on spherical- and disk-shaped particles.[38, 39] In those studies, the optimum thickness of the C-m-WO$_3$ and H-h-WO$_3$ sensors was observed to be quite different, which probably results from the quite different morphology and surface structure of the sensing films.

We also noticed many surface defects exist on a single H-h-WO$_3$ particle (Fig. 4). NO$_2$ gas was observed to be easily adsorbed and reacted at the surface of the H-h-WO$_3$ at relatively low temperature, which would be associated with the presence of the surface defects.

Crystal structure features

It has been reported that the hexagonal WO$_3$ is a metastable crystal phase; impurities are necessary in stabilizing its crystal structure.[31,40-42] The as-synthesized WO$_3$ samples were investigated by solid state ^{1}H and ^{13}C NMR. ^{1}H-CRAMPS NMR spectra shown in Fig. 9 (a) indicated the presence of peaks of protons in the H-h-WO$_3$, which were located at 4.2, 3.3, and 0.9 ppm, while no proton was detected in the C-m-WO$_3$. The peak at 4.2 ppm was assigned to NH$_4^+$ ions by comparison with the ^{1}H NMR spectrum of the starting material (NH$_4$)$_{10}$W$_{12}$O$_{41}$·5H$_2$O, where the peak of NH$_4^+$ was obvious. The weak shoulder between 4 and 6 ppm in the spectrum of H-h-WO$_3$ may be given by surface and structure H$_2$O molecules.[41,43-45] The signal at 0.9 ppm was assigned to the surface-bonded OH groups, in accordance with previous works.[45,46] We suppose that the peak at 3.3 ppm may probably come from the residual surfactant, CTAB, which was introduced in the hydrothermal treatment for the H-h-WO$_3$ sample, however it was difficult to assign it only by ^{1}H NMR spectra. Then ^{13}C-DDMAS NMR measurements were carried out to get further structural information. The ^{13}C NMR spectra shown in Fig. 9 (b) indicated that no peak was detected in the C-m-WO$_3$ sample, while for H-h-WO$_3$ sample, peaks located at 65.6 and 52.7 ppm and signals lower than 30.5 ppm were observed. By comparison with the spectrum of pure CTAB, the peaks at 65.6 and 52.7 ppm were assigned to -CH$_2$-N and -N(CH$_3$)$_3$, respectively. The

signals lower than 30.5 ppm may originate from the –CH_3 and –CH_2– chains of CTAB,[47,48] where some observed differences in the chemical shift from pure CTAB can be explained in terms of the local bonding and environmental changes and/or the long-term field drift during the measurements.[49,50] Further detailed studies and analysis are in progress.
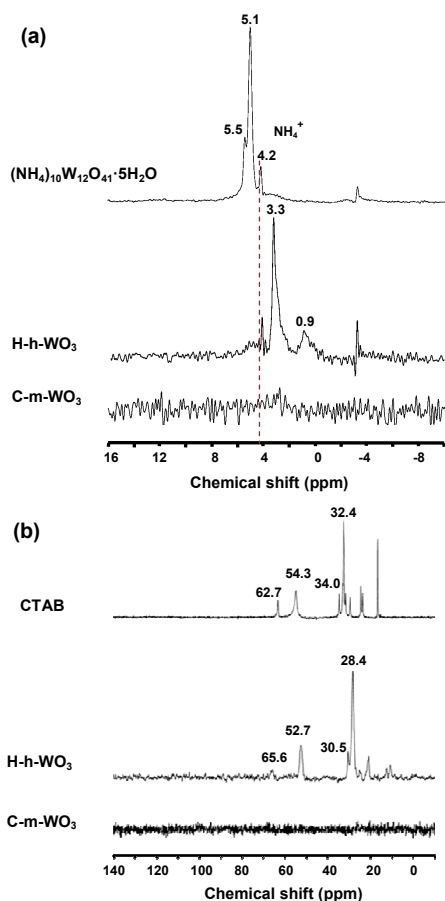

Figure 9. (a) ^{1}H-CRAMPS NMR spectra of C-m-WO$_3$, H-h-WO$_3$ and (NH$_4$)$_{10}$W$_{12}$O$_{41}$ · 5H$_2$O, and (b) ^{13}C-DDMAS NMR spectra of C-m-WO$_3$, H-h-WO$_3$ and CTAB.
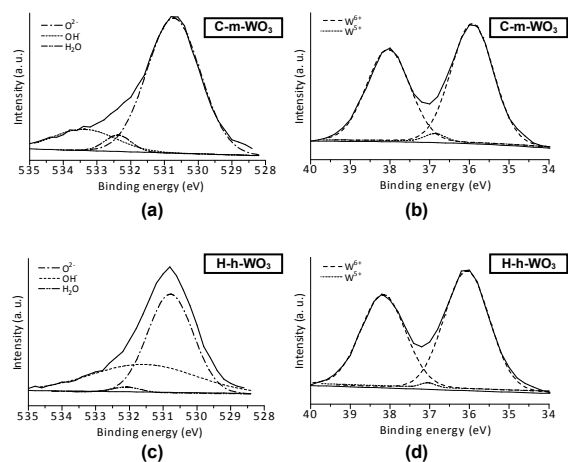

Figure 10. XPS spectra of as-prepared C-m-WO$_3$: (a) O 1s, (b) W 4f; and H-h-WO$_3$: (c) O 1s, (d) W 4f.

The different oxidation states of tungsten were confirmed by XPS spectra (Fig. 10). Table S1 shows that the as-prepared H-h-WO$_3$ is almost completely oxidized with 99.3 % W^{6+} atoms detected (W$_{4f7/2}$ peak: 38.2, 37.0 eV; W4f$_{5/2}$ peak: 36.1 eV). However, the as-prepared C-m-WO$_3$ contained W^{6+} (98.3 %) and W^{5+} (1.7 %) species (W4f$_{7/2}$ peak: 38.0, 36.9 eV; W4f$_{5/2}$ peak: 35.9 eV). The amounts of surface species (O^{2-}, OH$^-$, and H$_2$O) were also examined. Table S1 shows that the amount of surface OH$^-$ was considerably larger for H-h-WO$_3$ (O^{2-}/OH$^-$/H$_2$O (in %) = 60.0/38.1/1.9) than for C-m-WO$_3$ (80.4/4.9/14.7).

NMR and XPS spectroscopy gave important information about the different crystal structures of C-m-WO$_3$ and H-h-WO$_3$. It was found that the small amount of residual impurities and cations were not only necessary to stabilize the H-h-WO$_3$ structure, but also without them, the H-h-WO$_3$ particles could not even be formed.[27,32,41] Morphology and structure transformation of tungstic acid hydrate, H$_2$WO$_4$·nH$_2$O, have been reported,[40] in which sodium ion content in the solid phase had been found to control the reaction route in the hydrothermal treatment of tungstic acid hydrates. In the present study, for synthesizing the H-h-WO$_3$ particles, relatively low temperature and the short-time acidification are necessary. It is reasonable to consider that residual NH$_4$$^+$ existing as a persistent contaminant in the reaction product, helps to form hexagonal crystal seeds, and plays an important role in forming the hexagonal WO$_3$ crystal in further hydrothermal treatment.[50] Surfactant CTAB is considered to adhere to the surface of the WO$_6$ octahedra or the structure water and to affect differently the growing rates of different crystal planes of the precursors, appearing as the preferred preferentially oriented (2 0 0) plane in Fig. 2. During the hydrothermal process, morphology formation and recrystallization occur at an accelerated rate in the autoclave. With the presence of the hexagonal crystal seeds and the controlled orientation direction, as shown in Fig. 11, the hexagonal-plate-like H-h-WO$_3$ particles were finally formed. However, until now we could not succeed in preparing pure H-h-WO$_3$ in our experiments. The more detailed quantitative explanation on the crystallization and composition of the H-h-WO$_3$ needs further investigation. On the other hand, due to the presence of minor amount of residual impurities and cations in the hexagonal WO$_3$, it is assumed that reduced tungsten atoms such as W^{5+} and/or W^{4+} may also present to maintain the electroneutrality.[27,32,40-42] However, the XPS spectra showed that the as-prepared H-h-WO$_3$ was almost completely oxidized. The reason is supposed to be due to the presence of OH$^-$, which contributed to maintain the electroneutrality in H-h-WO$_3$ crystal structure. The small amount of W^{5+} atoms detected in C-m-WO$_3$ samples in this study may be due to a change of the sample surface in the high vacuum in an XPS chamber, in accordance with previous works.[32,41] The high density of surface OH$^-$ species and the presence of residual impurities and cations in the crystal structure may result in the increased conductance and recombination sites in the H-h-WO$_3$ particles, which greatly affect the adsorption of the gas molecules as well as the transport of electrons, leading to make a definite influence on the sensing properties of the H-h-WO$_3$ sensor.
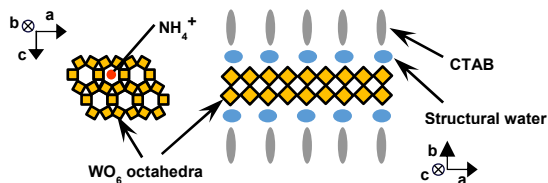

Figure 11. Schematic model for the formation of H-h-WO$_3$ particles during the hydrothermal process. WO$_6$ octahedra is extracted from the reported model.[31]

Conclusions

Influence of the morphology (cuboid or hexagonal-plate) and crystal structure (monoclinic or hexagonal) of WO_3 on gas-sensing properties was studied. Thin- and thick-film sensors based on two kinds of WO_3 (C-m-WO_3 and H-h-WO_3) were fabricated and NO_2 sensing properties were investigated. The C-m-WO_3 thin-film sensor (2.19 μm thick) showed the extremely high sensor responses of 160 to 20-ppb NO_2 and 10120 to 500-ppb NO_2 at 200 °C, which may possess great potential for actual applications in very highly sensitive, environmental NO_2 monitoring. The large specific surface area and the high crystallinity of the C-m-WO_3 may also imply the potential as a promising candidate for designing high activity photocatalyst materials. On the other hand, the H-h-WO_3 formed a porous-structure sensing film, and the higher sensor response was obtained in the operation of the H-h-WO_3 thick-film sensor (14.4 μm thick) than the C-m-WO_3 thick-film one (11.5 μm thick). Solid state ^1H and ^{13}C NMR spectra indicated the presence of residual impurities and cations in the as-synthesized H-h-WO_3 sample, and higher density of OH^- on the surface of H-h-WO_3 particles was demonstrated by XPS spectra. Stabilizing impurities and defects in the crystal structure as well as the surface OH^- density will be key factors to understand the different sensing properties of the H-h-WO_3 and C-m-WO_3 gas sensors.

Acknowledgements

Notes and references

[a] Department of Applied Chemistry, College of Life Sciences, Ritsumeikan University, 1-1-1 Noji-higashi, Kusatsu, Shiga 525-8577, Japan, *E-mail:kojimaka@sk.ritsumei.ac.jp

[b] Graduate School of Science and Technology, Kumamoto University, 2-39-1 Kurokami, Chuo-ku, Kumamoto, Kumamoto 860-8555, Japan

[c] Department of Materials Science and Engineering, National Institute of Technology, Suzuka College Shiroko, Suzuka, Mie 510-0294, Japan

[d] Comprehensive Analysis Center, the Institute of Scientific and Industrial Research, Osaka University, 8-1 Mihogaoka, Ibaraki, Osaka 567-0047, Japan

† Electronic Supplementary Information (ESI) available: [details of any supplementary information available should be included here]. See DOI: 10.1039/b000000x/

1. E. Comini, G. Faglia, G. Sberveglieri, D. Calestani, L. Zanotti, M. Zha, *Sens. Actuators B*, 2005, **111**, 2-6.
2. Y.B. Shen, T. Yamazaki, Z.F. Liu, D. Meng, T. Kikuta, N. Nakatani, M. Saito, M. Mori, *Sens. Actuators B*, 2009, **135**, 524-529.
3. Q. Wan, Q.H. Li, Y.J. Chen, T.H. Wang, X.L. He, J.P. Li, C.L. Lin, *Appl. Phys. Lett.*, 2004, **84**, 3654-3656.
4. C. Li, D.J. Zhang, X.L. Liu, S. Han, T. Tang, C.W. Zhou, *Appl. Phys. Lett.*, 2003, **83**, 1845-1847.
5. A. Ponzoni, E. Comini, G. Sberveglieri, J. Zhou, S.Z. Deng, N.S. Xu, Y. Ding, Z.L. Wang, *Appl. Phys. Lett.*, 2006, **88**, 203101.
6. C.S. Rout, A. Govindaraj, C.N.R. Rao, *J. Mater. Chem.*, 2006, **16**, 3936-3941.
7. C. Santato, M. Odziemkowski, M. Ulmann, J. Augustynski, *J. Am. Chem. Soc.*, 2001, **123**, 10639-49.
8. R. Abe, H. Takami, N. Murakami, B. Ohtani, *J. Am. Chem. Soc.*, 2008, **130**, 7780-7781.
9. Q. Xiang, G.F. Meng, H.B. Zhao, Y. Zhang, H. Li, W.J. Ma, J.Q. Xu, *J. Phys. Chem. C*, 2010, **114**, 2049-2055.
10. B. Xue, J. Peng, Z. Xin, Y. Kong, L. Li, B. Li, *J. Mater. Chem.*, 2005, **15**, 4793-4798.
11. S. Wang, X. Feng, J. Yao, L. Jiang, *Angew. Chem. Int. Ed.*, 2006, **45**, 1264–1267.
12. J. Wang, E. Khoo, P.S. Lee, J. Ma, *J. Phy. Chem. C*, 2008, **112**, 14306-14312.
13. I.M. Szilagyi, S. Saukko, J. Mizsei, A.L. Toth, J. Madarasz, G. Pokol, *Solid State Sci.*, 2010, **12**, 1857-1860.
14. M. Akiyama, J. Tamaki, N. Miura, N. Yamazoe, *Chem. Lett.*, 1991, **20**, 1611-1614.
15. N. M. Vuong, H. Jung, D.J. Kim, H. Kim, S.K. Hong, *J. Mater. Chem.*, 2012, **22**, 6716-6725.
16. Z. Liu, M. Miyauchi, T. Yamazaki, Y. Shen, *Sens. Actuators B*, 2009, **140**, 514–519.
17. D. Meng, T. Yamazaki, Y. Shen, Z. Liu, T. Kikuta, *Appl. Surface Sci.*, 2009, **256**, 1050-1053.
18. Z. Meng, C. Kitagawa, A. Takahashi, Y. Okochi, J. Tamaki, *Sens. Mater.*, 2009, **5**, 259-264.
19. L. You, X. He, D. Wang, P. Sun, Y.F. Sun, X.S. Linag, Y. Du, G.Y. Lu, *Sens. Actuators B*, 2012, **173**, 426–432.
20. L. You, Y.F. Sun, J. Ma, Y. Guan, J.M. Sun, Y. Du, G.Y. Lu, *Sens. Actuators B*, 2011, **157**, 401–407.
21. T. Kida, A. Nishiyama, M. Yuasa, K. Shimanoe, N. Yamazoe, *Sens. Actuators B*, 2009, **135**, 568–574.
22. S. Ashraf, C.S. Blackman, R.G. Palgrave, S.C. Naisbitt, I.P. Parkin, *J. Mater. Chem.*, 2007, **17**, 3708-3713.
23. P.V. Tong, N.D. Hua, V.V. Quang, N.V. Duy, N.V. Hieu, *Sens. Actuators B*, 2013, **183**, 372–380.
24. D. Meng, N.M. Shaalan, T. Yamazaki, T. Kikuta, *Sens. Actuators B*, 2012, **169**, 113–120.
25. B. Cao, J. Chen, X. Tang, W. Zhou, *J. Mater. Chem.*, 2009, **19**, 2323-2327.
26. A. Ponzoni, E. Comini, G. Sberveglieri, J. Zhou, S.Z. Deng, N.S. Xu, Y. Ding, Z.L. Wang, *Appl. Phys. Lett.*, 2006, **88**, 203101-203103.
27. I.M. Szilágyi, L. Wang, P.-I. Gouma, C. Balázsi, J. Madarász, G. Pokol, *Materials Research Bulletin*, 2009, **44**, 505-508.
28. I.M. Szilágyi, S. Saukko, J. Mizsei, P. Király, G. Tárkányi, A.L. Szabó, K.V. Josepovits, J. Madarász, G. Pokol, *Mater. Sci. Forum*, 2008, **589**, 161-166.
29. C. Balázsi, L. Wang, E.O. Zayim, I.M. Szilágyi, K. Sedlacková, J. Pfeifer, A.L. Tóth, P.-I. Gouma, *Journal of the European Ceramic Society*, 2008, **28**, 913-917.
30. L. Wang, J. Pfeifer, C. Balázsi, I.M. Szilágyi, P.I. Gouma, *Proc. of SPIE 2007*, 2007, **6769**, 67690E-1-8.
31. I.M. Szilágyi, J. Madarász, G. Pokol, P. Király, G. Tárkányi, S. Saukko, J. Mizsei, A.L. Tóth, A. Szabó, K.V. Josepovits, *Chem. Mater.*, 2008, **20**, 4116-4125.
32. T. Firkala, B. Fórizs, E. Drotár, A. Tompos, A.L. Tóth, K.V. Josepovits, K. László, M. Leskelä, I.M. Szilágyi, *Catalysis Letters*, 2014, **144**, 831-836.
33. D. Chen, L. Gao, A. Yasumori, K. Kuroda, Y. Sugahara, Small, 2008, **4**, 1813-1822.
34. Z. Meng, T. Hashishin, J. Tamaki, K. Kojima, *Key Engineering Materials*, 2013, **538**, 308-311.
35. N. Yamazoe, G. Sakai, K. Shimanoe, *Catalysis Surveys from Asia*, 2003, **7**, 63-75.
36. H. Xia, Y. Wang, F. Kong, S. Wang, B. Zhu, Z. Guo, J. Zhang, Y. Wang, S. Wu, *Sens. Actuators B*, 2008, **134**, 133–139.
37. C.Y. Lee, S.J. Kim, I.S. Hwang, J.H. Lee, *Sens. Actuators B*, 2009, **142**, 236–242.
38. J. Tamaki, A. Hayashi, Y. Yamamoto, M. Matsuoka, *Sens. Actuators B*, 2003, **95**, 111–115.
39. J. Tamaki, A. Hayashi, Y. Yamamoto, *J. Ceram. Soc. Jpn., PacRim5 Special Issue*, 2004, **112**, S546–S549.
40. C. Balazsi, J. Pfeifer, *Solid State Ionics*, 2002, **151**, 353-358.
41. I.M. Szilágyi, B. Fórizs, O. Rosseler, Á. Szegedi, P. Németh, P. Király, G. Tárkányi, B. Vajna, K.V. Josepovits, K. László, A.L. Tóth, P. Baranyai, M. Leskelä, *J. Catalysis*, 2012, **294**, 119-127.
42. I.M. Szilágyi, I. Sajó, P. Király, G. Tárkányi, A.L. Tóth. A. Szabó, K. Varga-Josepovits, J. Madarász, G. Pokol, *J Therm Anal Calorim*, 2009, **98**, 707-716.
43. I.M. Szilágyi, J. Madarász, G. Pokol, F. Hange, G. Szalontai, K. Varga-Josepovits, and A.L. Tóth, *J Therm Anal Calorim*, 2009, **97**, 11-18.
44. I.M. Szilágyi, F. Hange, J. Madarász, and G. Pokol, *J. Inorg. Chem.*, 2006, 3413-3418.
45. H.-J. Lunk, M. Salmen, D. Heidemann, *International J. Refractory Matals & Hard Materials*, 1998, **16**, 23-30.
46. H.-J. Lunk, B. Ziemer, M. Salmen, D. Heidemann, *Refractory Matals & Hard Materials*, 1993-1994, **12**, 17-26.
47. C. Sizun, J. Raya, A. Intasiri, A. Boos, K. Elbayed, *Microporous and Mesoporous Mater.*, 2003, **66**, 27-36.
48. W. Shen, J. Yang, S. Li, W. Hu, J. Xu, H. Zhang, Q. Zou, L. Chen, F. Deng, *Microporous and Mesoporous Mater.*, 2010, **127**, 73-81.
49. N. Chaiyut, T. Amornsakchai, H. Kaji, F. Horii, *Polymer*, 2006, **47**, 2470-2481.
50. Y. Koyama, T. Takao, Y. Yanagisawa, H. Nakagome, M. Hamada, T. Kiyoshi, H. Takahashi, H. Maeda, *Physica C*, 2009, **469**, 694-701.
51. J.H. Ha, P. Muralidharan, D.K. Kim, *J. Alloys Compd.*, 2009, **475**, 446-451.